Geophysical Research Letters

RESEARCH LETTER

10.1029/2025GL118671

Key Points:

- Both extreme positive and negative IOD (EXpIOD/EXnIOD) tend to enhance late-season monsoon rainfall over western South Asia (WSA)
- Asymmetry in rainfall and SST patterns between EXpIOD and EXnIOD induces the WSA rainfall response via asymmetric moisture convergence
- Extreme IOD's asymmetry also affects the WSA soil moisture and air temperature, basically independently of ENSO forcing

Supporting Information:

Supporting Information may be found in the online version of this article.

Correspondence to:

J.-Z. Wang and H. Fan,
jia-zhen_wang@foxmail.com;
fanhj8@mail.sysu.edu.cn

Citation:

Xie, M., Wang, J.-Z., Fan, H., Zhang, L., & Chen, Z. (2025). Asymmetric impacts of extreme positive and negative Indian Ocean Dipole events on late-summer monsoon rainfall in Western South Asia. *Geophysical Research Letters*, *52*, e2025GL118671. https://doi.org/10.1029/2025GL118671

Received 8 AUG 2025
Accepted 11 NOV 2025

Asymmetric Impacts of Extreme Positive and Negative Indian Ocean Dipole Events on Late-Summer Monsoon Rainfall in Western South Asia

Mingmei Xie[1], Jia-Zhen Wang[1,2], Hanjie Fan[3,4], Lei Zhang[5], and Zhaohui Chen[1]

[1]Frontier Science Center for Deep Ocean Multispheres and Earth System, and Physical Oceanography Laboratory, Ocean University of China, Qingdao, China, [2]Laoshan Laboratory, Qingdao, China, [3]School of Atmospheric Sciences, Sun Yat-sen University, and Southern Marine Science and Engineering Guangdong Laboratory (Zhuhai), Zhuhai, China, [4]Guangdong Province Key Laboratory for Climate Change and Natural Disaster Studies, Sun Yat-sen University, Zhuhai, China, [5]State Key Laboratory of Tropical Oceanography, South China Sea Institute of Oceanology, Chinese Academy of Sciences, Guangzhou, China

Abstract Observations show a fragile linear relationship between South Asian monsoon rainfall and the Indian Ocean Dipole (IOD), reflecting their complex interactions. Our analysis reveals that both extreme positive and negative IOD (EXpIOD/EXnIOD) events could enhance rainfall over western South Asia during August–September, even when ENSO signals are removed. This asymmetric influence arises from moisture convergence driven by anomalous winds. AGCM simulations indicate that EXpIOD-related suppressed convection over the eastern pole induces a westward-extended Gill-type anticyclone, whose southwesterlies reinforce the background monsoon and promote orographic rainfall near the Western Ghats. Contrastingly, EXnIOD features an eastward-shifted dipole; positive convection in the east drives a cyclonic circulation that transports Bay of Bengal moisture westward. This flow converges with cross-equatorial southwesterlies generated by the western pole, enhancing rainfall over western India. These results suggest that the pattern asymmetry between EXpIOD and EXnIOD is a key factor that deserves consideration when assessing IOD-monsoon interactions.

Plain Language Summary Summer monsoon rainfall over South Asia (SA) profoundly impacts regional agriculture and disaster risks. The Indian Ocean Dipole (IOD), whose lifecycle overlaps the monsoon season, has been widely examined for its nearby influence on SA rainfall. Yet observational evidence suggests no clear linear correlation between the IOD index and late monsoon rainfall (August–September). Here we demonstrate that both extreme positive and negative IOD events (EXpIOD/EXnIOD) tend to enhance rainfall over western SA (WSA), indicating a nonlinear relationship. During EXpIOD, westward-extended negative rainfall anomalies over the eastern Indian Ocean trigger an elongated anticyclone, whose southwesterly winds strengthen the background monsoon flow, advecting moisture into WSA. In contrast, EXnIOD events feature an eastward-shifted dipole pattern, with cyclonic circulation centered over the Bay of Bengal. Anomalous easterlies transport moisture westward and merge with cross-equatorial southerlies associated with suppressed convection over the western Indian Ocean. This confluence drives moisture convergence and rainfall over WSA. Asymmetric impacts can also be detected in other variables, like soil moisture and surface temperature. These findings underscore that, beyond the IOD phase, the spatial structure of its SST and rainfall anomalies effectively modulates the monsoon response and may serve as a valuable predictor for late-season rainfall over WSA.

1. Introduction

The Indian Ocean is bounded by vast landmasses to its north, creating a favorable configuration where land–sea thermal contrast and orographic forcing from surrounding high plateaus together give rise to the vigorous South Asian monsoon system (Acosta & Huber, 2020; Krishnamurti, 1971; Wu et al., 2012). This imparts pronounced seasonality to ambient interannual variability (Li et al., 2003; Xiang et al., 2011). During the boreal summer (June to September, JJAS), the South Asian summer monsoon (SASM) contributes approximately 70%–90% of the annual rainfall across the Indian subcontinent (Hrudya et al., 2021; Parthasarathy et al., 1994). The lifecycle of the SASM can be divided into two sub-seasons: the early season (June–July, JJ) and the late season (August–September, AS). Studies have indicated that these two sub-seasons exhibit distinct atmospheric circulation patterns and driving mechanisms (Boschat et al., 2011; Kawamura et al., 2005; Kothawale & Kulkarni, 2015; Terray et al., 2003).

In the same season, the Indian Ocean exhibits another interannual climate mode known as the Indian Ocean Dipole (IOD), characterized by a seesaw pattern in sea surface temperature anomalies (SSTAs; Saji et al., 1999; Webster et al., 1999). Positive IOD (pIOD) events feature warmer SSTAs in the western Indian Ocean (WIO) and cooler SSTAs in the east (EIO), while negative events generally show the reverse pattern. The IOD typically initiates in JJ, intensifies during AS, and peaks around October (Saji et al., 1999). Given its temporal alignment and geographic location neighboring the monsoon region, the IOD has been widely studied for its potential influence on monsoon rainfall (see Cherchi et al., 2021; Hrudya et al., 2021 for reviews). Since the intensities of monsoon rainfall during JJ and AS are not significantly correlated (Ghosh et al., 2018; Terray et al., 2003), and the AS season coincides more closely with the mature phase of IOD, this study primarily focuses on the AS period hereafter.

However, long-term analyses indicate that the linear relationship between the IOD and SASM rainfall is rather weak (Ashok et al., 2001; Saji et al., 1999). This relationship is further complicated by the spatial heterogeneity in monsoon rainfall responses (Behera & Ratnam, 2018). As an illustration, regressing AS mean precipitation anomalies onto the simultaneous dipole mode index (DMI) yields statistically insignificant results across the Indian subcontinent (Figure 1a). Nevertheless, case studies have demonstrated that EXpIOD events can enhance monsoon rainfall over the western Indian Peninsula by inducing anomalous southwesterly winds that transport moisture inland (e.g., Ratna et al., 2021). Supporting this, the 1994 and 1997 EXpIOD events were linked to increased precipitation, with the 1997 event partially offsetting the concurrent El Niño-induced drought conditions (Ashok & Saji, 2007; Gadgil et al., 2004; Ratna et al., 2024). Interestingly, in contrast to EXpIOD events, the 2010 extreme negative IOD (EXnIOD) event was also associated with above-average monsoon rainfall over northwestern India and Pakistan (Horii et al., 2013; Priya et al., 2015), suggesting that both EXpIOD and EXnIOD events may lead to enhanced precipitation, albeit through different mechanisms.

These observations imply that the relationship between the IOD and monsoon rainfall is complex and influenced by multiple factors. One potential factor is interference from concurrent El Niño–Southern Oscillation (ENSO) events (Gadgil et al., 2004; Hrudya et al., 2021; Mahendra et al., 2024; Ratna et al., 2024). This study will employ partial regression analyses and numerical modeling to isolate the effects of ENSO. Another consideration is the inherent asymmetry between extreme IOD events (Xie, Wang, Zhang, Han, et al., 2025). Specifically, EXpIOD events often exhibit stronger amplitudes, particularly in the EIO (Hong et al., 2008). Their associated EIO cooling (and dry anomaly) tends to center off Sumatra and extends further westward (Figure S1a in Supporting Information S1). In contrast, the counterpart warming of EXnIOD is confined near Java (Figure S1b in Supporting Information S1; Xie, Wang, Zhang, Han, et al., 2025). Such asymmetries in amplitude and spatial pattern (Figure S1c in Supporting Information S1) may disrupt the linear assumptions commonly used to relate IOD phases to monsoon rainfall. However, the mechanisms by which IOD asymmetry influences SASM rainfall remain inadequately understood. India and Pakistan are densely populated, agriculture-dependent countries, where variations in rainfall, soil moisture, and temperature exert a strong influence on agricultural production (Gadgil & Kumar, 2006; Li et al., 2023). Understanding the complex relationship between extreme IOD events and late-season monsoon rainfall over western South Asia (WSA) will help improve climate-informed decision-making and enhance the resilience of regional farming systems and livelihoods.

2. Data and Methods

2.1. Observational and Reanalysis Data Sets

To narrow down estimation errors in large-scale SST and precipitation, we used the averaged data sets of NOAA Optimum Interpolated SST version 2 (OISSTv2; Huang et al., 2021) and NCEP Global Ocean Data Assimilation System (GODAS; Behringer & Xue, 2004) for SST, along with the averaged NOAA CPC Merged Analysis of Precipitation (CMAP; Xie & Arkin, 1997) and Global Precipitation Climatology Project (GPCP; Adler et al., 2003) data sets for rainfall. The analysis period spanned from 1982 to 2022. Concurrent three-dimensional atmospheric variables were provided by the Japanese 55-year Reanalysis (JRA-55; Kobayashi et al., 2015). Soil moisture, converted to water-height equivalents, was obtained from the CPC Monthly Data set, Version 2 (Fan & van den Dool, 2004). All anomalies were calculated relative to the monthly climatology over the entire data period and subsequently linearly detrended.

2.2. Moisture Budget Analysis

A moisture budget analysis (Trenberth & Guillemot, 1995) was performed to show the dominant processes driving the asymmetric rainfall patterns associated with EXpIOD and EXnIOD events. For each grid, the vertically integrated moisture budget, expressed in pressure coordinates, is given by:

$$P' - E' = -\langle \nabla \cdot \mathbf{u}'_h \bar{q} \rangle - \langle \nabla \cdot \bar{\mathbf{u}}_h q' \rangle - \langle \nabla \cdot \mathbf{u}'_h q' \rangle + R, \tag{1}$$

where angle brackets represent mass-weighted vertical integration over the entire atmospheric column; P denotes total precipitation; E is evaporation; $\mathbf{u}_h$ denotes horizontal winds; q is specific humidity; and R is the residual term.

We further calculated the moisture transport across each boundary of the WSA region (65°–75°E, 10°–30°N; red box in Figure 1a). Equation 1 can be integrated as follows (Chakraborty & Singhai, 2021):

$$\iint (P' - E')\, dA = \underbrace{-\oint \langle \mathbf{u}'_h \bar{q} \rangle dl}_{\text{dynamic}} \underbrace{-\oint \langle \bar{\mathbf{u}}_h q' \rangle dl}_{\text{thermodynamic}} \underbrace{-\oint \langle \mathbf{u}'_h q' \rangle dl}_{\text{nonlinear}} + R, \tag{2}$$

where l denotes the contour integral along the lateral boundaries of the WSA region.

2.3. Model Simulations

We used the dry linear baroclinic model (LBM; Watanabe & Kimoto, 2000) to demonstrate idealized asymmetric atmospheric responses induced by the differential rainfall patterns associated with EXpIOD and EXnIOD events. The model was configured with a T42 horizontal resolution and 20 vertical sigma levels. The background state was set to the AS mean climatology. The centers of heating were estimated based on the observed rainfall pattern, with details provided in Text S1 of Supporting Information S1.

We also analyzed large-ensemble Atmospheric Model Intercomparison Project (AMIP)-type experiments conducted by the NCAR Community Atmosphere Model version 5 (CAM5), to highlight the deterministic, SST-forced SASM rainfall response from additive internal atmospheric variability. In these global AMIP (GOGA) experiments, the lower boundary conditions were prescribed globally using observed SST and sea ice concentration, along with time-varying radiative forcing. A total of 60 ensemble members were generated. The analysis period covers 1982–2014. The ensemble-mean AMIP results enable attribution of significant rainfall anomalies to SST forcing, thereby providing a foundation for the subsequent sensitive experiments.

To further isolate the contribution of extreme IOD events from the global SST forcing, particularly to remove the influence of concurrent ENSO signals embedded in the AMIP simulations, we conducted a set of SST-forced sensitive experiments using CAM5. The CAM5 was forced with observed composite SSTAs associated with EXpIOD and EXnIOD events over the tropical Indian Ocean (40°–120°E, 15°S–15°N; excluding the South China Sea) from May to the following April. Each sensitive experiment was integrated for 30 years, and the ensemble mean of the final 20 years was used for analysis. Details of these CAM5 sensitive experiments and an additional heating prescribed experiment are described in Text S1 of Supporting Information S1.

3. Results

3.1. Characterizing Extreme IOD Events

Given the air–sea coupled nature of IOD and the presence of asymmetries in both oceanic and atmospheric variables, we performed a multivariate empirical orthogonal function (MV-EOF) analysis on the AS mean anomalies of SST and precipitation. Specifically, standardized SST and precipitation anomalies from the same year were concatenated into a single block matrix and subjected to EOF decomposition. SST and precipitation fields were then regressed separately onto the resulting principal component (PC) time series to obtain their respective spatial patterns.

The first leading mode (MV-EOF1) captures the canonical IOD pattern common to events (Figures 1c and 1e), with stronger loadings concentrated in the EIO. Physically, this mode reflects the growth of IOD under the Bjerknes positive feedback (Li et al., 2003; Saji et al., 1999), so that the associated oceanic and atmospheric

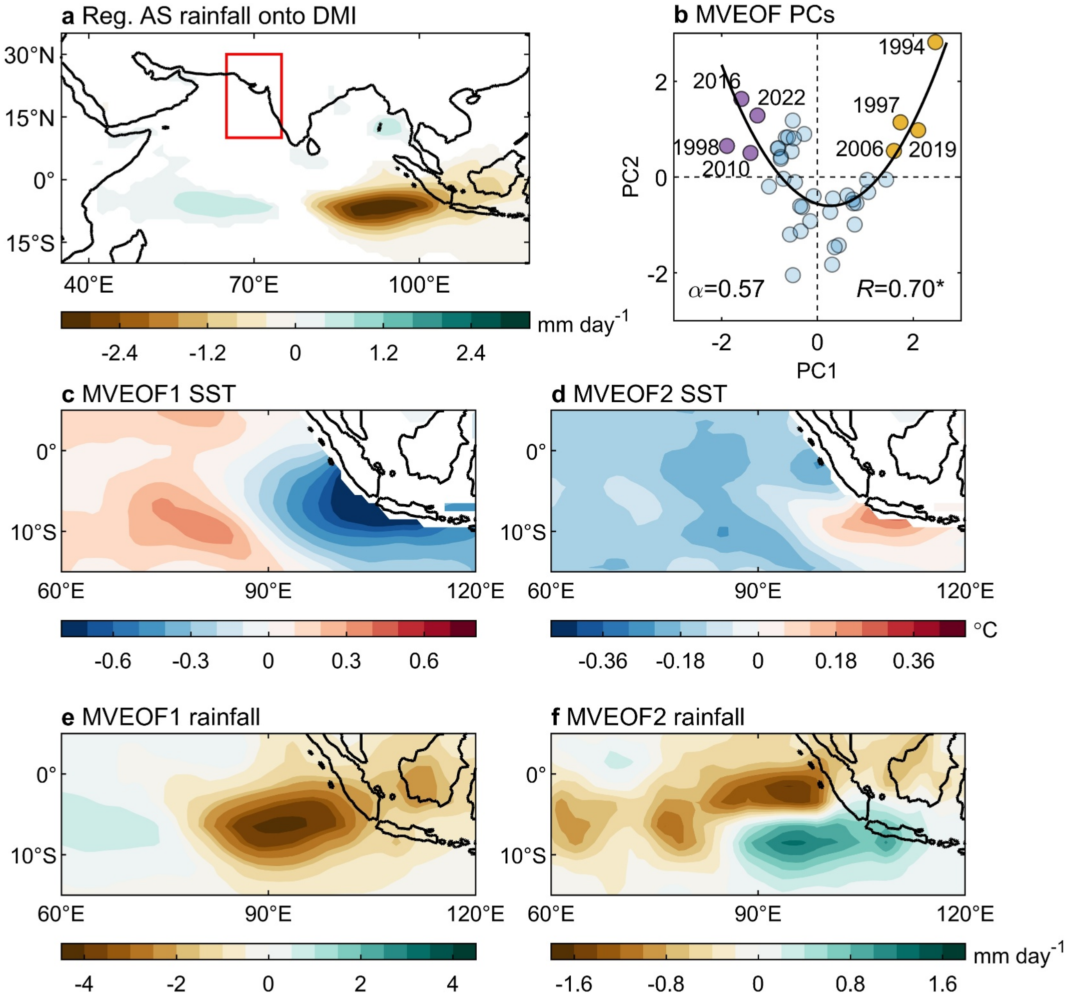

Figure 1. The two leading MV-EOF modes over the EIO. (a) AS rainfall anomalies (shading; mm day^{-1}) regressed onto the DMI. The DMI represents the SSTA gradient between the WIO (50°–70°E, 10°S–10°N) and EIO (90°–110°E, 10°S–0°; Saji et al., 1999). Only results significant at the 90% confidence level are shown. The red box indicates the region for subsequent diagnosis. (b) Scatterplot of standardized PC1 and PC2 from the MV-EOF in phase space, with EXpIOD events shown as yellow dots and EXnIOD events as purple dots. The fractional variances explained by these two modes are 67% and 10%, respectively. The nonlinear relationship between PC1 and PC2 is represented by the black fitted curve, with the quadratic parameter α indicated. (c) MV-EOF1-related SSTA (shading; °C) over the EIO, obtained by regressing AS SSTA onto the PC1 decomposed over the 75°–110°E, 10°S–0° region. This region is selected because significant spatially asymmetric signals are largely confined to the eastern basin (Figure S1 in Supporting Information S1; Xie, Wang, Zhang, Han, et al., 2025). Panel (d) As in panel (c), but based on regression onto the PC2. (e), (f) MVEOF-related rainfall patterns (shading; mm day^{-1}), obtained by regressing AS rainfall anomalies onto (e) PC1 and (f) PC2, respectively.

variables show opposite-signed anomalies between the two IOD phases (i.e., symmetric to phases). Correspondingly, the PC1 is highly correlated with the DMI ($R = 0.95$) and exhibits comparable positive skewness (~+0.54). However, relying on MV-EOF1 and its associated PC1 can only describe the temporal evolution of a fixed spatial pattern. They are insufficient to depict spatial differences from the canonical structure that characterize extreme IOD events (Cai et al., 2021; Wang et al., 2024).

The second mode (MV-EOF2) complements this limitation, featuring a pronounced meridional dipole structure across the EIO (Figures 1d and 1f). Physically, when the IOD reaches extreme amplitudes (i.e., large |PC1| values), nonlinear interactions among anomalies become increasingly important. Previous studies have shown that nonlinear zonal and vertical thermal advection generates additional cooling along the equator and off Sumatra during both positive and negative extremes (Xie, Wang, Zhang, Han, et al., 2025). Because this nonlinear advection always acts as a cooling effect, it introduces a phase-independent asymmetry: during EXpIOD events, the enhanced cooling shifts SST anomalies northward and westward (corresponding to the northern negative lobe of MV-EOF2), while during EXnIOD events, it suppresses the equatorward expansion of warm anomalies, confining them to the southeastern sector (corresponding to the southern positive lobe of MV-EOF2). Similar nonlinear moisture advection processes also contribute to the spatial separation of anomalous rainfall centers between EXpIOD and EXnIOD events (Xie, Wang, Zhang, Han, et al., 2025).

The asymmetric behavior of nonlinear advection amplifying during extreme events provides physical support for the quadratic dependence of MV-PC2 on MV-PC1 (Figure 1b). Indeed, PC2 can be approximated by a quadratic function of PC1:

$$\mathrm{PC2}(t)^{*} = \alpha \mathrm{PC1}(t)^{2} + \beta \mathrm{PC1}(t) + \gamma, \tag{3}$$

with the fitted PC2* correlating at 0.7 ($p < 0.01$) with the observed PC2. Based on this characteristic, we define EXpIOD events (1994, 1997, 2006, 2019) as those with PC1 > +1 standard deviation (s.d.) and PC2 > +0.5 s.d., and EXnIOD events (1998, 2010, 2016, 2022) as those with PC1 < −1 s.d. And PC2 > +0.5 s.d. When both PCs are positive, as in EXpIOD events, the two leading modes positively superimpose, producing a northward- and westward-displaced cold SSTA and associated dry conditions off Sumatra (Figure 2a; Figure S1a in Supporting Information S1). In contrast, during EXnIOD events, characterized by a negative MV-EOF1 and a positive MV-EOF2, the warm and wet anomalies shift southeastward, with centers near Java (Figure 2b; Figure S1b in Supporting Information S1). This two-mode classification approach thus unifies the amplitude-based definition of IOD extremes with their pattern asymmetry, providing a more comprehensive description of IOD spatial diversity.

3.2. Asymmetric Impacts on Late-Summer Monsoonal Rainfall

From a broader perspective, the suppressed EIO convection during EXpIOD events can extend westward beyond 80°E, with its northern boundary reaching close to the equator. Its concomitant enhanced rainfall center appears over the western basin near 55°E (Figure 2a). The suppressed convection induces a Gill-type atmospheric response, generating a pair of anticyclonic circulations to its west (Gill, 1980). The northern branch of this circulation converges toward the Western Ghats and enhances precipitation over adjacent regions.

By contrast, the atmospheric anomaly pattern associated with EXnIOD events is not a simple mirror image of that during EXpIOD events. The enhanced convection on the eastern side is mostly confined east of 80°E and remains about 4° south of the equator, while the suppressed rainfall over the western basin is centered around 65°E (Figure 2b). The EXnIOD heating induces a Gill-type anomalous cyclone centered over the Bay of Bengal (BoB) and simultaneously excites a Rossby wave train, leading to the development of a mid-tropospheric high-pressure anomaly over the Tibetan Plateau (Li & Mu, 2001; Xu et al., 2023). Under the established pressure gradient, strong easterlies form on the northern flank of the cyclone, transporting moisture westward along the Indo-Gangetic Plain (Singh et al., 2022). As a result, EXnIOD events also correspond to significantly enhanced rainfall over WSA.

In the composite asymmetry field, the most prominent features are a meridional dipole of rainfall anomalies over the EIO, reminiscent of MV-EOF2, and increased rainfall anomalies over WSA (Figure 2c), including Gujarat, Rajasthan, Maharashtra, Punjab, and Sindh (Figure S2a in Supporting Information S1). This distinct phase-independent asymmetry appears to weaken the linear relationship between DMI and Indian monsoonal rainfall. When the quadratic PC2* component is removed from the original precipitation anomalies (Dommenget et al., 2013):

$$\mathrm{Pr}'_{\mathrm{res}}(x, y, t) = \mathrm{Pr}'_{\mathrm{ori}}(x, y, t) - k(x, y) \times \mathrm{PC2}^{*}(t), \tag{4}$$

where $k(x,y)$ represents the local regression coefficient at each gridpoint, the composite asymmetry in WSA rainfall disappears along with the spatial asymmetry between EXpIOD and EXnIOD patterns (Figure S3 in Supporting Information S1). This result implies a potential linkage between the two asymmetric features. In contrast, when PC2* is replaced by the Pacific Niño3.4 index, those asymmetric rainfall signals remain evident (Figure S4 in Supporting Information S1), suggesting that it is intrinsic to extreme IOD events rather than being induced by ENSO, and thus warrants further investigation.

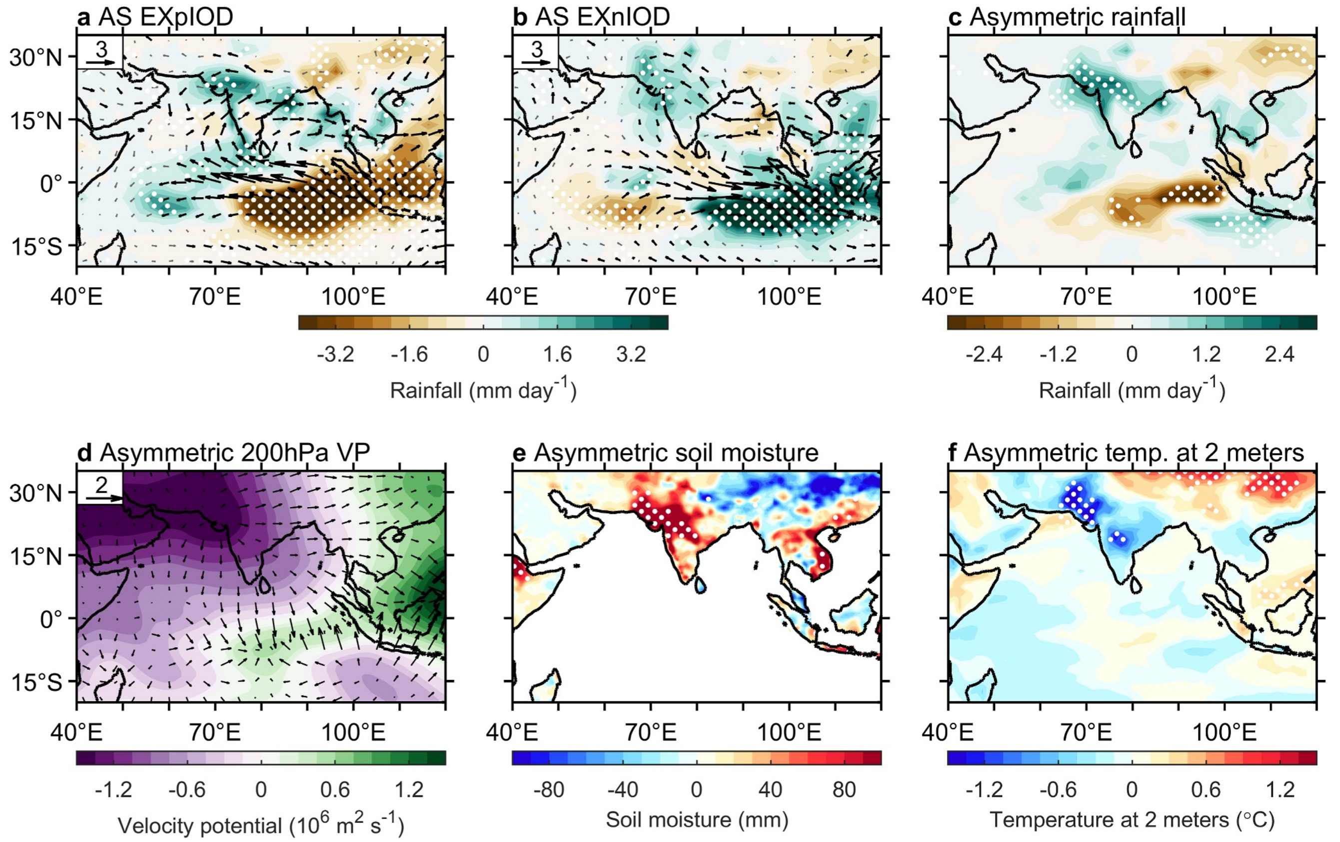

Figure 2. Asymmetric components of atmospheric variables during extreme IOD events. (a) Composites of AS rainfall anomalies (shading; mm day^{-1}) and 850-hPa winds anomalies (vectors; m s^{-1}) during EXpIOD years. Significant values at the 90% confidence level based on the *t*-test are stippled by white dots. The vectors significant at the 90% confidence level based on the *t*-test are shown in bold black. Panel (b) As in panel (a), but for EXnIOD years. (c) Asymmetric rainfall component between (a, b), defined as the sum of the EXpIOD and EXnIOD composites (i.e., EXpIOD + EXnIOD). Significant values at the 90% confidence level based on a Monte Carlo resampling method (see Text S2 in Supporting Information S1) are stippled by white dots. (d) Spatially asymmetric component of 200-hPa velocity potential (shading; 10^6 m^2 s^{-1}) and divergent wind (vectors; m s^{-1}) during extreme IOD events. Note that since the velocity potential satisfies the global mean of zero, its values are not solely determined by local divergence. Therefore, significance testing is not performed on it. Instead, our focus here is on its gradient (i.e., the divergent winds). Panels (e, f) As in panel (d), but for (e) soil moisture anomalies (mm), and (f) anomalous temperature at 2 m (°C).

Imprints of rainfall asymmetry are also significant in the asymmetric responses of other relevant variables. Accordingly, an upper-tropospheric meridional dipole in velocity potential emerges over the EIO, along with a pronounced divergence center over WSA (Figure 2d). Increased rainfall leads to locally enhanced soil moisture (Figure 2e). In addition, the accompanying increase in cloud cover reduces incoming shortwave radiation and thereby weakens radiative heating at the surface. Combined with the enhanced latent cooling effect from increased evapotranspiration due to higher soil moisture (Seneviratne et al., 2010), these processes result in a cold near-surface air temperature anomaly over WSA (Figure 2f).

Previous research indicates that moderate rainfall increases can boost pearl millet production in India, especially in the northwestern states of Rajasthan, Gujarat, and Maharashtra (Reddy et al., 2013; Singh et al., 2017). On average, this is reflected in nationally elevated millet production during both EXpIOD and EXnIOD years (Figures S2b and S2c in Supporting Information S1). In contrast, for the climatically drier Pakistan, excessive rainfall tends to trigger flooding, adversely affecting rice production in key producing regions such as Punjab and Sindh (Abbas & Mayo, 2021; Rehman & Ahmad, 2022). Consequently, extreme IOD years are associated with reduced rice output in Pakistan on average (Figure S2b and S2d in Supporting Information S1).

3.3. Mechanisms: Asymmetric Moisture Transport Linked to Extreme IOD Rainfall Patterns

Moisture budget analysis over WSA (red box in Figure 3) reveals that, for both EXpIOD and EXnIOD events (Figures 3a and 3d), the dominant contributor to enhanced precipitation during the late SASM season is the

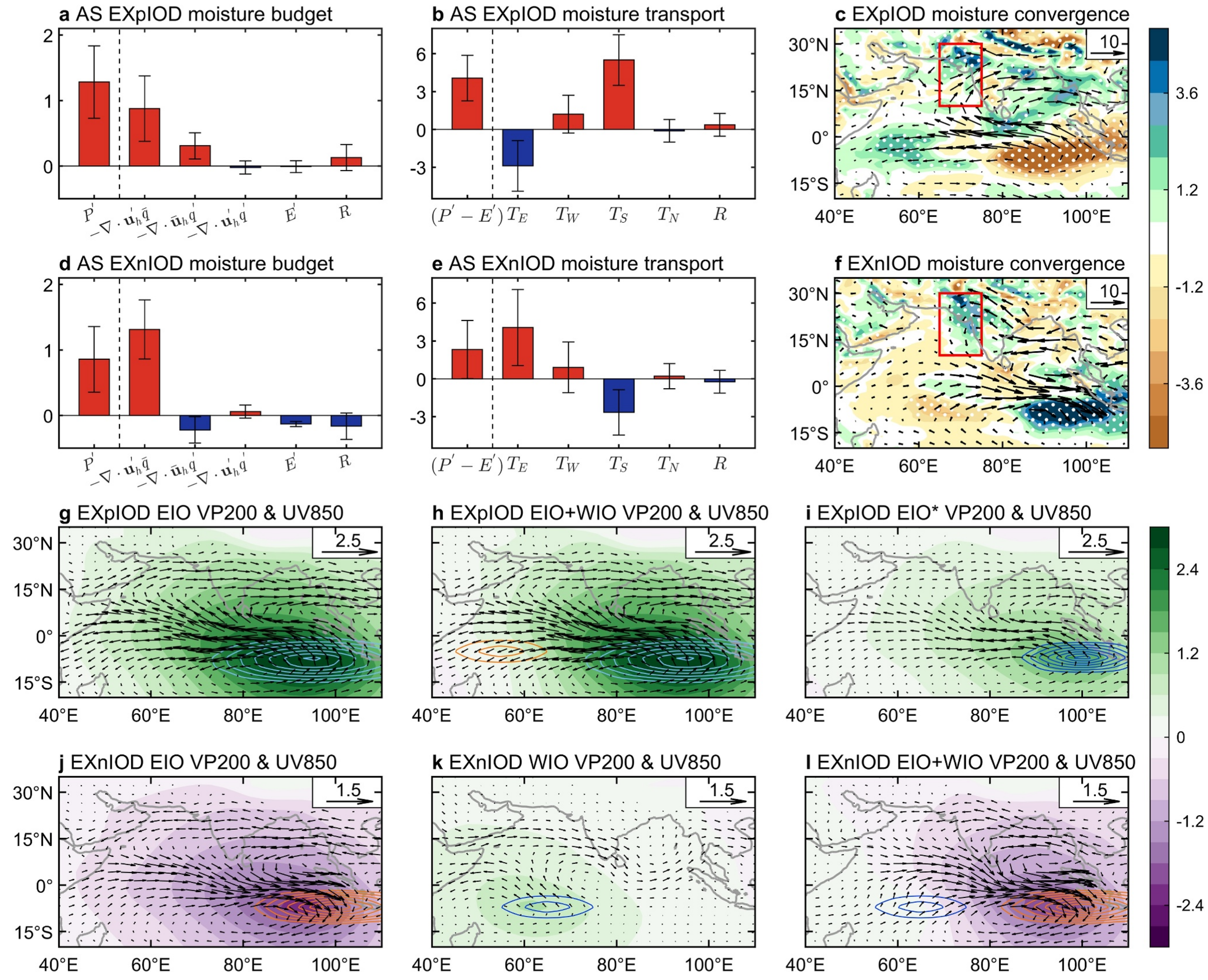

Figure 3. Moisture budget analysis and LBM experiments for EXpIOD and EXnIOD events. (a) Moisture budget terms (mm day^{-1}) for EXpIOD over the region 65°–75°E, 10°–30°N (red box in Figure 3c; Equation 1). (b) Net moisture transport into the diagnosed region across the eastern ($\boldsymbol{T_E}$), western ($\boldsymbol{T_W}$), southern ($\boldsymbol{T_S}$), and northern ($\boldsymbol{T_N}$) boundaries (10^7 kg s^{-1}), calculated from the dynamic term. The results based on the full form of Equation 2 are presented in Figure S6 of Supporting Information S1. (c) Moisture flux anomalies induced by anomalous winds ($\mathbf{u}'_h\bar{\boldsymbol{q}}$; vectors; 10^6 kg m^{-1} s^{-1}) and their convergence (shading; mm day^{-1}) during EXpIOD events. Significant values at the 90% confidence level based on the *t*-test are indicated by white stippling. Panels (d–f) As in panels (a–c), but for EXnIOD events. (g) Responses of 850-hPa winds (vectors; m s^{-1}) and 200-hPa velocity potential (shading; 10^6 m^2 s^{-1}) in the LBM experiment forced by idealized diabatic heating over the EIO during EXpIODs. Panel (h) As in panel (g), but forced by diabatic heating over both the WIO and EIO during EXpIODs, indicating that the EIO dominates the responses. Panel (i) Same amplitude as in panel (g), but the diabatic heating is shifted eastward and southward to 85°–115°E, 12°–2°S (EIO*). (j) Responses of 850-hPa winds (vectors; m s^{-1}) and 200-hPa velocity potential (shading; 10^6 m^2 s^{-1}) in the LBM experiment forced by diabatic heating over the EIO during EXnIODs. Panel (k) As in panel (j), but forced by diabatic heating over the WIO during EXnIODs. (l) Combined response of EIO and WIO. In panels (g–l), blue and red contours represent regions of negative and positive diabatic heating imposed in the LBM, respectively, with contours spaced at intervals of 0.9 K day^{-1}.

convergence of climatological moisture by anomalous horizontal winds, represented by the term $-\langle\nabla\cdot\mathbf{u}'_h\bar{q}\rangle$. Spatially, this term closely mirrors the distribution of rainfall anomalies (Figures 3c and 3f). In contrast, the secondary term—the convergence of anomalous moisture advected by the mean wind ($-\langle\nabla\cdot\bar{\mathbf{u}}_h q'\rangle$)—plays an opposite role in EXpIOD and EXnIOD events, as q' varies in phase with SSTAs in the WIO, which are largely symmetric across opposite IOD phases (Figure S5 in Supporting Information S1). This result raises a new question: why does anomalous wind-driven moisture transport consistently result in convergence over WSA for both extreme phases? To address this, we shift the perspective from gridpoint-based moisture budget analysis Equation 1 to examining moisture transports across the lateral boundaries of the diagnosed region Equation 2.

The results indicate that moisture transports and their asymmetry are primarily governed by the dynamic term. In contrast, the thermodynamic component contributes nearly symmetrically between phases and is of much smaller magnitude, while the nonlinear term is negligible (Figure S6 in Supporting Information S1). During EXpIOD events, moisture inflow through the southern and western boundaries exceeds the outflow through the eastern boundary, resulting in net moisture accumulation (Figure 3b). This accumulation is closely tied to the anticyclonic Gill-type response north of the equator (Figure 3c). The southwesterly anomalies associated with this anticyclone align with the climatological monsoon flow, effectively transporting moisture-laden air through the southern and western boundaries. As these southwesterlies encounter the Western Ghats and are blocked from further eastward movement by the Himalayas, the airflow is forced upward by orographic lifting, leading to enhanced precipitation along the windward slopes.

This mechanism is broadly consistent with previous case attribution studies (e.g., Ratna et al., 2021). However, we further emphasize the key role of the westward-extended rainfall suppression during EXpIOD events in anchoring low-level convergence over western India. This is supported by LBM sensitive experiments: when the imposed heat source mimics the westward-extended precipitation anomaly pattern observed during EXpIODs, the resulting anticyclonic circulation extends westward into the WIO and induces strong westerly flow toward the Indian subcontinent (Figures 3g and 3h). In contrast, when the heat source with the same amplitude is confined eastward and southward, resembling a moderate pIOD, the resulting anticyclone is centered over the BoB (Figure 3i), and the westerly flow over the Arabian Sea is substantially weaker, failing to generate strong orographically forced convergence.

During EXnIOD events, moisture inflow from the eastern and western boundaries of the diagnostic region exceeds outflow to the south, resulting in a net moisture surplus (Figure 3e). Spatially, the easterly flow transporting moist air from the BoB veers southward along the western flank of the Indian subcontinent. As a result, there is no apparent outflow across the western boundary. Moreover, this northerly flow merges with cross-equatorial southerlies near the southern tip of India to form westerlies roughly parallel to the region's southern boundary, thereby further reducing southward outflow (Figure 3f).

To understand why the anomalous wind field takes this configuration during EXnIOD events, we conducted a series of idealized LBM experiments. First, prescribing diabatic heating solely over the EIO reproduces a cyclonic Gill-type response (Figure 3j). Because the heat source is positioned relatively eastward and southward, the cyclone is centered over the BoB, and its northern flank generates easterlies that spread across the Indian subcontinent (Figure 3j). Nevertheless, this setup alone cannot fully account for the observed weak moisture outflow (Figure 3f).

A key structural difference during EXnIOD is that the western pole of the dipole pattern is shifted eastward compared to EXpIOD. When diabatic cooling associated with the western pole is imposed in the LBM, it triggers an anticyclone and cross-equatorial southwesterlies that develop northward toward the Indian subcontinent (Figure 3k). These winds partially offset the easterly anomalies induced by the eastern pole convection and help steer the low-level flow back toward the EIO (Figure 3l), thereby limiting moisture export through both the southern and western boundaries. When diabatic forcing from both poles is combined, the simulated wind matches the observed pattern (Comparing Figure 3l with Figure 3f). Therefore, the eastward-shifted rainfall dipole accounts for the distinctive winds during EXnIOD and promotes moisture convergence over WSA.

3.4. SST-Forced Numerical Model Validation

The contrasting rainfall patterns between EXpIOD and EXnIOD events are related to differences in their respective SSTA structures. To overcome the limitation of insufficient observational samples and to demonstrate that the response to SST forcing can emerge above atmospheric internal variability, we turn to AGCM experiments for support.

In the GOGA experiment, both EXpIOD and EXnIOD events are associated with enhanced rainfall over WSA. For EXpIOD events, the anomalous rainfall is primarily attributed to the anticyclonic circulation that supplies abundant moisture and convergence over the Indian Peninsula (Figure 4a). In contrast, during EXnIOD events, the enhancement is related to a broad cyclonic anomaly over the BoB. Its consequent easterly winds merge with cross-equatorial southerlies to produce moisture convergence (Figure 4b). The most prominent signal in the

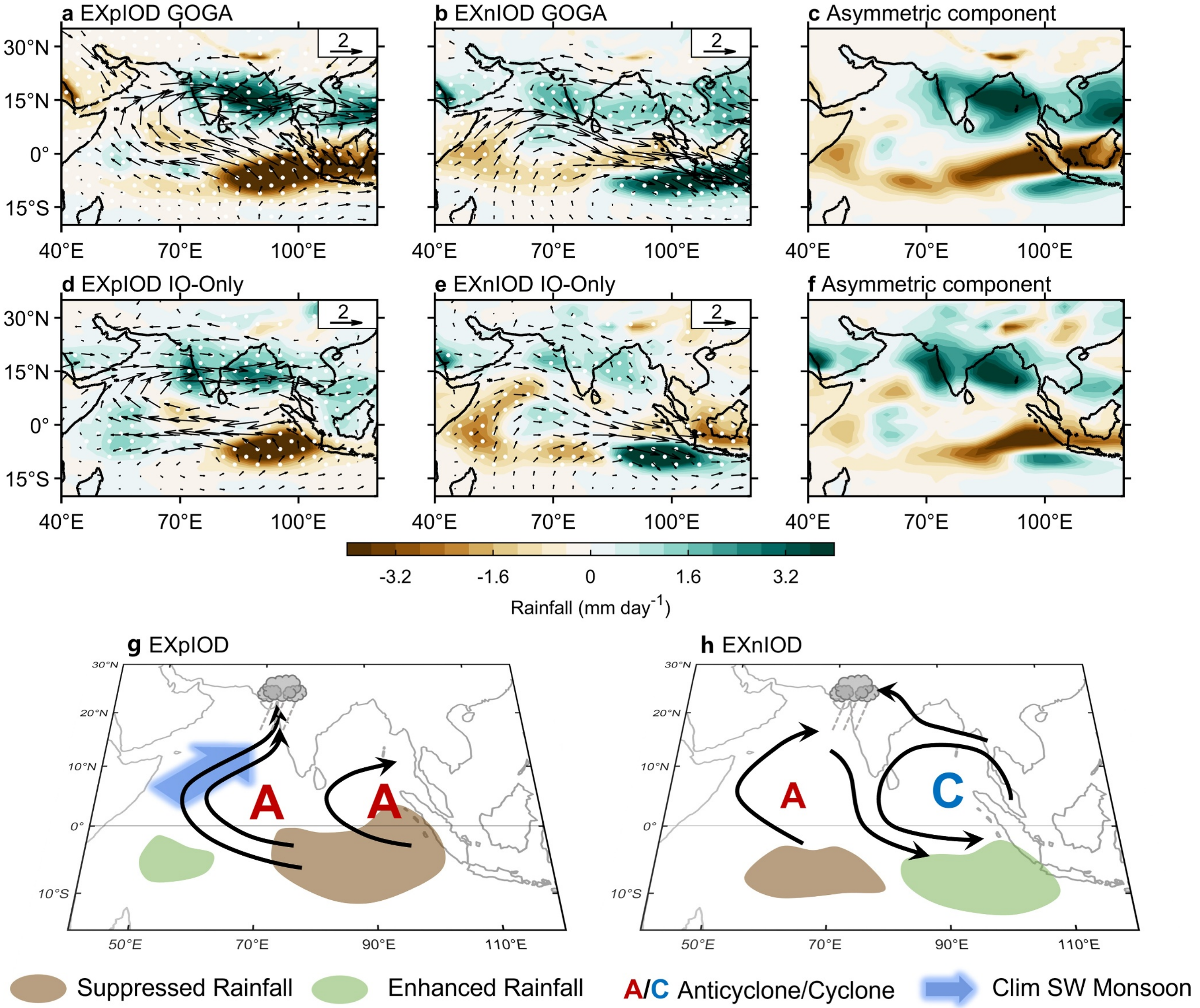

Figure 4. Comparison between CAM5 GOGA and IO-only experiments. (a) Composite AS mean rainfall anomalies (shading; mm day^{-1}) and 850-hPa wind anomalies (vectors; m s^{-1}) during EXpIOD events in GOGA simulations. Significant values at the 90% confidence level based on the Student's *t*-test are stippled by white dots. Panel (b) As in panel (a), but for EXnIOD events. (c) Asymmetric component of rainfall anomalies, defined as the sum of (a, b). (d) Differences in AS mean rainfall (shading; mm day^{-1}) and 850-hPa winds (vectors; m s^{-1}) between the EXpIOD IO-only experiment and the control run of CAM5. Significant values at the 90% confidence level based on the Student's *t*-test are stippled by white dots. Panel (e) As in panel (d), but for the EXnIOD IO-only experiment. (f) Asymmetric component of IO-only-simulated rainfall anomalies (shading; mm day^{-1}), computed as the sum of (d, e). (g, h) Schematic diagrams illustrating the asymmetric SASM rainfall response induced by EXpIOD and EXnIOD.

asymmetric rainfall component is a meridional dipole over the central to EIO, accompanied by positive anomalies over WSA (Figure 4c).

To further isolate the effect of Indian Ocean SST forcing, an experiment (IO-only) was conducted by prescribing only the observed composite SSTAs associated with EXpIOD and EXnIOD events. Results show that EXpIOD induces suppressed convection over the EIO that extends more westward and reaches close to the equator compared with negative events, while EXnIOD corresponds a dry anomaly in the WIO that is shifted farther eastward, both consistent with observations (Figures 4d and 4e). Consequently, in the IO-only experiment, EXpIOD enhances rainfall over WSA via a Gill-type anticyclonic circulation, while EXnIOD achieves similar effects through the confluence of easterly anomalies across the Indian subcontinent and cross-equatorial flows.

The IO-only results confirm that Indian Ocean SST forcing alone can induce an asymmetric SASM rainfall response, and the associated rainfall anomalies closely resemble those in the GOGA experiment (Figure 4f).

Because the GOGA experiment is forced with global SST, the effects of co-occurring ENSO signals are inherently included—EXpIOD events often coincide with El Niño, while EXnIOD events tend to co-occur with La Niña (Xie, Wang, Zhang, & Chen, 2025; Xie, Wang, Zhang, Han et al., 2025). A comparison between the GOGA and IO-only experiments reveals the modulation effect of ENSO on SASM rainfall. Rainfall over WSA in Figure 4a is weaker than in Figure 4d, whereas rainfall in Figure 4b is stronger than in Figure 4e. This indicates that El Niño tends to suppress, while La Niña tends to enhance, concurrent monsoon rainfall, consistent with the well-known negative correlation between ENSO and SASM (e.g., Ashok et al., 2001). These results further suggest that the influence of ENSO on SASM rainfall is basically linear, while the relationship between extreme IOD events and SASM rainfall exhibits a pronounced nonlinearity.

4. Conclusions and Discussion

4.1. Conclusions

In this study, we identify a pronounced pattern asymmetry between EXpIOD and EXnIOD events during the late SASM season. This asymmetry manifests as a meridional dipole in SST–rainfall anomalies over the central–EIO (i.e., MV-EOF2), along with a nonlinear relationship between the leading two PCs. This means a more northwestward-displaced EXpIOD anomalous centers and a more southeastward-shifted EXnIOD centers. Composite analyses reveal that, beyond spatial differences in tropical centers, both EXpIOD and EXnIOD events are associated with enhanced rainfall over WSA, and this asymmetric rainfall response is also reflected in divergent winds, soil moisture, and surface air temperature.

The common underlying mechanism lies in the convergence of moisture induced by anomalous horizontal winds ($-\langle \nabla \cdot \mathbf{u}_h' \overline{q} \rangle$). Specifically, during EXpIOD events, the negative rainfall anomalies in the EIO are located closer to the equator and extend farther west, generating a westward-expanded Gill-type anticyclonic response. The resulting low-level southwesterly anomalies transport abundant moisture toward WSA (Figure 4g). In contrast, during EXnIOD events, the eastern-pole rainfall anomalies are positioned farther east and south, while the western pole also shifts eastward. This leads to a cyclonic Gill-type response centered over the BoB, with easterlies on its northern flank transporting moisture westward. These flows merge with cross-equatorial southwesterlies linked to the western pole, again promoting moisture convergence over the region (Figure 4h). Thus, the spatial asymmetry of extreme IOD events leads to asymmetric circulation and convergence patterns, which in turn result in their asymmetric influence on SASM rainfall.

4.2. Discussions

This asymmetric rainfall response provides a potential explanation for the weak or insignificant linear correlation often observed between traditional IOD indices (e.g., DMI or MV-EOF PC1) and SASM rainfall (Figure 1a). Because both EXpIOD and EXnIOD tend to enhance monsoon rainfall, their effects cancel out in linear regressions (Figure 1a). Moreover, when isolating events with modestly positive PC1 ($\mathrm{PC1} > 0.25$ s.d.) and notably negative PC2 ($\mathrm{PC2} < -0.5$ s.d.)—corresponding to some moderate pIOD events (1982, 1987, 1999, 2003, 2015, and 2018; Cai et al., 2021; Wang et al., 2024)—we find that their rainfall anomaly pattern resembles the reversal of MV-EOF2 (Figure S7a in Supporting Information S1), especially after regressing out the influence of MV-EOF1 (Figure S7b in Supporting Information S1). These moderate pIOD events exhibit suppressed rainfall west of Java, accompanied by positive anomalies to the north and west, indicating a southeastward contraction of rainfall suppression and enhanced rainfall over the central Indian Ocean compared to EXpIOD. Interestingly, this dipole pattern is associated with reduced rainfall over WSA (Figures S7a and S7b in Supporting Information S1).

Recall that the positive phase of MV-EOF2 (Figure 2c) is associated with increased rainfall over WSA, while the negative phase corresponds to reduced rainfall (Figure S7b in Supporting Information S1). This pattern suggests a potentially linear relationship between MV-EOF2 and WSA rainfall variability. Further supporting this, a correlation between the regional mean rainfall over WSA and full-field rainfall anomalies (after removing ENSO effects) yields a dipole-like pattern resembling that of MV-EOF2 (Figure S7c in Supporting Information S1). This indicates that MV-EOF2 effectively captures IOD-related WSA rainfall variability that is independent of the ENSO signal.

Furthermore, when diabatic heating anomalies derived from MV-EOF2 rainfall structures are imposed on the climatological heating profile in CAM5 (Text S1 in Supporting Information S1), the model reproduces enhanced rainfall over WSA, confirming the physical relevance of MV-EOF2 to monsoon rainfall variability (Figure S8 in Supporting Information S1). Taken together, our findings highlight that the importance of considering not only IOD polarity but also the spatial configuration of SST and rainfall anomalies when using the IOD as an explanatory factor of SASM variability.

Conflict of Interest

The authors declare no conflicts of interest relevant to this study.

Data Availability Statement

The OISSTv2 (Huang et al., 2021), GODAS (Behringer & Xue, 2004), CMAP (Xie & Arkin, 1997), GPCP (Adler et al., 2003), and CPC soil moisture (Fan & van den Dool, 2004) data sets are available from the NOAA PSL website: https://psl.noaa.gov/data/gridded/data.noaa.oisst.v2.html, https://psl.noaa.gov/data/gridded/data.godas.html, https://psl.noaa.gov/data/gridded/data.cmap.html, https://psl.noaa.gov/data/gridded/data.gpcp.html, https://psl.noaa.gov/data/gridded/data.cpcsoil.html. JRA-55 data (Kobayashi et al., 2015) are available from: https://doi.org/10.5065/D60G3H5B (Japan Meteorological Agency, 2013). Indian pearl millet production data are available from the Indian Institute of Millets Research: https://www.milletstats.com/download-center/. Pakistani rice production data are available from the Agriculture Marketing Information Service, Punjab: http://www.amis.pk/Agristatistics/production.aspx. CAM5 GOGA experiments can be accessed via the NCAR Geoscience Data Exchange: https://doi.org/10.5065/D6J101D1 (Kay et al., 2021) and NOAA PSL repository (Murray et al., 2020): https://downloads.psl.noaa.gov/Projects/iccdata1/FACTS/.

Acknowledgments
This study is supported by the National Natural Science Foundation of China project (42306001), the Postdoctoral Fellowship Program of CPSF under Grant GZB20250217, the China Postdoctoral Science Foundation under Grants 2025M770881 and 2025T180247, Project SDCX-ZG-202502030 Funded by Postdoctoral Innovation Program of Shandong Province, and the development fund of South China Sea Institute of Oceanology of the Chinese Academy of Sciences (SCSIO202203). LZ is supported by the National Natural Science Foundation of China project (42376021).

References

Abbas, S., & Mayo, Z. A. (2021). Impact of temperature and rainfall on rice production in Punjab, Pakistan. *Environment, Development and Sustainability*, *23*(2), 1706–1728. https://doi.org/10.1007/s10668-020-00647-8

Acosta, R. P., & Huber, M. (2020). Competing topographic mechanisms for the summer Indo-Asian monsoon. *Geophysical Research Letters*, *47*(3), e2019GL085112. https://doi.org/10.1029/2019GL085112

Adler, R. F., Huffman, G. J., Chang, A., Ferraro, R., Xie, P.-P., Janowiak, J., et al. (2003). The Version-2 Global Precipitation Climatology Project (GPCP) monthly precipitation analysis (1979–Present) [Dataset]. *Journal of Hydrometeorology*, *4*(6), 1147–1167. https://doi.org/10.1175/1525-7541(2003)004<1147:TVGPCP>2.0.CO;2

Ashok, K., Guan, Z., & Yamagata, T. (2001). Impact of the Indian Ocean Dipole on the relationship between the Indian monsoon rainfall and ENSO. *Geophysical Research Letters*, *28*(23), 4499–4502. https://doi.org/10.1029/2001GL013294

Ashok, K., & Saji, N. H. (2007). On the impacts of ENSO and Indian Ocean dipole events on sub-regional Indian summer monsoon rainfall. *Natural Hazards*, *42*(2), 273–285. https://doi.org/10.1007/s11069-006-9091-0

Behera, S. K., & Ratnam, J. V. (2018). Quasi-asymmetric response of the Indian summer monsoon rainfall to opposite phases of the IOD. *Scientific Reports*, *8*(1), 123. https://doi.org/10.1038/s41598-017-18396-6

Behringer, D. W., & Xue, Y. (2004). Evaluation of the global ocean data assimilation system at NCEP: The Pacific Ocean [Dataset]. *Paper presented at the Eighth Symposium on Integrated Observing and Assimilation Systems for Atmosphere, Oceans, and Land Surface, Seattle, WA*. https://www.researchgate.net/publication/228856991_Evaluation_of_the_global_ocean_data_assimilation_system_at_NCEP_The_Pacific_Ocean

Boschat, G., Terray, P., & Masson, S. (2011). Interannual relationships between Indian summer monsoon and Indo-Pacific coupled modes of variability during recent decades. *Climate Dynamics*, *37*(5), 1019–1043. https://doi.org/10.1007/s00382-010-0887-y

Cai, W., Yang, K., Wu, L., Huang, G., Santoso, A., Ng, B., et al. (2021). Opposite response of strong and moderate positive Indian Ocean Dipole to global warming. *Nature Climate Change*, *11*(1), 27–32. https://doi.org/10.1038/s41558-020-00943-1

Chakraborty, A., & Singhai, P. (2021). Asymmetric response of the Indian summer monsoon to positive and negative phases of major tropical climate patterns. *Scientific Reports*, *11*(1), 22561. https://doi.org/10.1038/s41598-021-01758-6

Cherchi, A., Terray, P., Ratna, S. B., Sankar, S., Sooraj, K. P., & Behera, S. (2021). Chapter 8—Indian Ocean Dipole influence on Indian summer monsoon and ENSO: A review. In J. Chowdary, A. Parekh, & C. Gnanaseelan (Eds.), *Indian summer monsoon variability* (pp. 157–182). Elsevier.

Dommenget, D., Bayr, T., & Frauen, C. (2013). Analysis of the non-linearity in the pattern and time evolution of El Niño southern oscillation. *Climate Dynamics*, *40*(11), 2825–2847. https://doi.org/10.1007/s00382-012-1475-0

Fan, Y., & van den Dool, H. (2004). Climate Prediction center global monthly soil moisture data set at 0.5° resolution for 1948 to present [Dataset]. *Journal of Geophysical Research*, *109*(D10). https://doi.org/10.1029/2003JD004345

Gadgil, S., & Kumar, K. R. (2006). The Asian monsoon—Agriculture and economy. In B. Wang (Ed.), *The Asian monsoon* (pp. 651–683). Springer Berlin Heidelberg.

Gadgil, S., Vinayachandran, P. N., Francis, P. A., & Gadgil, S. (2004). Extremes of the Indian summer monsoon rainfall, ENSO and equatorial Indian Ocean oscillation. *Geophysical Research Letters*, *31*(12). https://doi.org/10.1029/2004GL019733

Ghosh, R., Chakraborty, A., & Nanjundiah, R. S. (2018). Relative role of pre-monsoon conditions and intraseasonal oscillations in determining early-vs-late Indian monsoon intensity in a GCM. *Theoretical and Applied Climatology*, *131*(1), 319–333. https://doi.org/10.1007/s00704-016-1970-z

Gill, A. E. (1980). Some simple solutions for heat-induced tropical circulation. *Quarterly Journal of the Royal Meteorological Society*, *106*(449), 447–462. https://doi.org/10.1002/qj.49710644905

Hong, C.-C., Li, T., LinHo, & Kug, J.-S. (2008). Asymmetry of the Indian Ocean dipole. Part I: Observational analysis. *Journal of Climate*, *21*(18), 4834–4848. https://doi.org/10.1175/2008JCLI2222.1

Horii, T., Ueki, I., Ando, K., & Mizuno, K. (2013). Eastern Indian Ocean warming associated with the negative Indian Ocean dipole: A case study of the 2010 event. *Journal of Geophysical Research: Oceans*, *118*(1), 536–549. https://doi.org/10.1002/jgrc.20071

Hrudya, P. H., Varikoden, H., & Vishnu, R. (2021). A review on the Indian summer monsoon rainfall, variability and its association with ENSO and IOD. *Meteorology and Atmospheric Physics*, *133*(1), 1–14. https://doi.org/10.1007/s00703-020-00734-5

Hu, P., Chen, S., Chen, W., & Tan, B. (2025). Asian–Pacific summer monsoon variability and atmospheric teleconnection patterns: Review and outlook. *Journal of Meteorological Research*, *39*(3), 651–672. https://doi.org/10.1007/s13351-025-4222-2

Huang, B., Liu, C., Banzon, V., Freeman, E., Graham, G., Hankins, B., et al. (2021). Improvements of the Daily Optimum Interpolation Sea Surface Temperature (DOISST) version 2.1 [Dataset]. *Journal of Climate*, *34*(8), 2923–2939. https://doi.org/10.1175/JCLI-D-20-0166.1

Japan Meteorological Agency. (2013). JRA-55: Japanese 55-year reanalysis, monthly means and variances [Dataset]. *Research Data Archive at the National Center for Atmospheric Research, Computational and Information Systems Laboratory*. https://doi.org/10.5065/D60G3H5B

Kawamura, R., Uemura, K., & Suppiah, R. (2005). On the recent change of the Indian summer Monsoon-ENSO relationship. *SOLA*, *1*, 201–204. https://doi.org/10.2151/sola.2005-052

Kay, J. E., Deser, C., Phillips, A. S., & Simpson, I. R. (2021). CESM1 large ensemble community Project [Dataset]. *NSF National Center for Atmospheric Research*. https://doi.org/10.5065/D6J101D1

Kobayashi, S., Ota, Y., Harada, Y., Ebita, A., Moriya, M., Onoda, H., et al. (2015). The JRA-55 reanalysis: General specifications and basic characteristics [Dataset]. *Journal of the Meteorological Society of Japan. Ser. II*, *93*(1), 5–48. https://doi.org/10.2151/jmsj.2015-001

Kothawale, D. R., & Kulkarni, J. R. (2015). Performance of August–September Indian monsoon rainfall when June–July rainfall is reported as being in deficit/excess. *Meteorology and Atmospheric Physics*, *127*(2), 147–161. https://doi.org/10.1007/s00703-014-0353-1

Krishnamurti, T. N. (1971). Tropical East-West circulations during the Northern summer. *Journal of the Atmospheric Sciences*, *28*(8), 1342–1347. https://doi.org/10.1175/1520-0469(1971)028<1342:TEWCDT>2.0.CO;2

Li, B., Zhou, L., Qin, J., Zhou, T., Chen, D., Hou, S., & Murtugudde, R. (2023). Middle east warming in spring enhances summer rainfall over Pakistan. *Nature Communications*, *14*(1), 7635. https://doi.org/10.1038/s41467-023-43463-0

Li, C., & Mu, M. (2001). The influence of the Indian Ocean dipole on atmospheric circulation and climate. *Advances in Atmospheric Sciences*, *18*(5), 831–843. https://doi.org/10.1007/BF03403506

Li, T., Wang, B., Chang, C. P., & Zhang, Y. (2003). A theory for the Indian Ocean dipole–zonal mode. *Journal of the Atmospheric Sciences*, *60*(17), 2119–2135. https://doi.org/10.1175/1520-0469(2003)060<2119:ATFTIO>2.0.CO;2

Mahendra, N., Chilukoti, N., Chowdary, J. S., & Renuka, S. (2024). A case study of deviant El Niño influence on the 2023 monsoon: An anecdote involving IOD, MJO and equivalent Barotropic Rossby waves. *Climate Dynamics*, *62*(8), 7185–7205. https://doi.org/10.1007/s00382-024-07273-4

Murray, D., Hoell, A., Hoerling, M., Perlwitz, J., Quan, X.-W., Allured, D., et al. (2020). Facility for Weather and Climate Assessments (FACTS): A community resource for assessing weather and climate variability [Dataset]. *Bulletin of the American Meteorological Society*, *101*(7), E1214–E1224. https://doi.org/10.1175/BAMS-D-19-0224.1

Parthasarathy, B., Munot, A. A., & Kothawale, D. R. (1994). All-India monthly and seasonal rainfall series: 1871–1993. *Theoretical and Applied Climatology*, *49*(4), 217–224. https://doi.org/10.1007/BF00867461

Priya, P., Mujumdar, M., Sabin, T. P., Terray, P., & Krishnan, R. (2015). Impacts of Indo-Pacific Sea surface temperature anomalies on the summer monsoon circulation and heavy precipitation over Northwest India–Pakistan Region during 2010. *Journal of Climate*, *28*(9), 3714–3730. https://doi.org/10.1175/JCLI-D-14-00595.1

Ratna, S. B., Cherchi, A., Osborn, T. J., Joshi, M., & Uppara, U. (2021). The extreme positive Indian Ocean dipole of 2019 and associated Indian summer monsoon rainfall response. *Geophysical Research Letters*, *48*(2), e2020GL091497. https://doi.org/10.1029/2020GL091497

Ratna, S. B., Sabeerali, C. T., Sharma, T., Pai, D. S., & Mohapatra, M. (2024). Combined influence of El Niño, IOD and MJO on the Indian Summer Monsoon Rainfall: Case Study for the years 1997 and 2015. *Atmospheric Research*, *299*, 107214. https://doi.org/10.1016/j.atmosres.2023.107214

Reddy, A. A., Rao, P. P., Yadav, O. P., Singh, I. P., Ardeshna, N. J., Kundu, K. K., et al. (2013). Prospects for *kharif* (Rainy season) and summer pearl millet in western India. *Working paper series no. 36. Patancheru*, ICRISAT. (pp. 302–324). http://oar.icrisat.org/id/eprint/6693

Rehman, F. U., & Ahmad, E. (2022). The effect of climate patterns on rice productivity in Pakistan: An application of Driscoll and Kraay estimator. *Environmental Science and Pollution Research*, *29*(35), 53076–53087. https://doi.org/10.1007/s11356-022-19624-x

Saji, N. H., Goswami, B. N., Vinayachandran, P. N., & Yamagata, T. (1999). A dipole mode in the tropical Indian Ocean. *Nature*, *401*(6751), 360–363. https://doi.org/10.1038/43854

Seneviratne, S. I., Corti, T., Davin, E. L., Hirschi, M., Jaeger, E. B., Lehner, I., et al. (2010). Investigating soil moisture–climate interactions in a changing climate: A review. *Earth-Science Reviews*, *99*(3), 125–161. https://doi.org/10.1016/j.earscirev.2010.02.004

Singh, R., Devi, G., Parmar, D. J., & Mishra, S. (2017). Impact of rainfall and temperature on the yield of major crops in Gujarat State of India: A Panel data analysis (1980–2011). *Current Journal of Applied Science and Technology*, *24*(5), 1–9. https://doi.org/10.9734/CJAST/2017/37071

Singh, R., Jaiswal, N., & Kishtawal, C. M. (2022). Rising surface pressure over Tibetan Plateau strengthens Indian summer monsoon rainfall over northwestern India. *Scientific Reports*, *12*(1), 8621. https://doi.org/10.1038/s41598-022-12523-8

Terray, P., Delecluse, P., Labattu, S., & Terray, L. (2003). Sea surface temperature associations with the late Indian summer monsoon. *Climate Dynamics*, *21*(7), 593–618. https://doi.org/10.1007/s00382-003-0354-0

Trenberth, K. E., & Guillemot, C. J. (1995). Evaluation of the global atmospheric moisture budget as seen from analyses. *Journal of Climate*, *8*(9), 2255–2272. https://doi.org/10.1175/1520-0442(1995)008<2255:EOTGAM>2.0.CO;2

Wang, J.-Z., Geng, T., Cai, W., Wang, G., Xie, M., Wu, L., & Chen, Z. (2024). Diverse responses of strong positive SST and rainfall Indian Ocean dipole events under greenhouse warming. *Journal of Climate*, *37*(16), 4133–4151. https://doi.org/10.1175/JCLI-D-23-0631.1

Watanabe, M., & Kimoto, M. (2000). Atmosphere-ocean thermal coupling in the North Atlantic: A positive feedback. *Quarterly Journal of the Royal Meteorological Society*, *126*(570), 3343–3369. https://doi.org/10.1002/qj.49712657017

Webster, P. J., Moore, A. M., Loschnigg, J. P., & Leben, R. R. (1999). Coupled ocean–atmosphere dynamics in the Indian Ocean during 1997–1998. *Nature*, *401*(6751), 356–360. https://doi.org/10.1038/43848

Wu, G., Liu, Y., He, B., Bao, Q., Duan, A., & Jin, F.-F. (2012). Thermal controls on the Asian summer monsoon. *Scientific Reports*, *2*(1), 404. https://doi.org/10.1038/srep00404

Xiang, B., Yu, W., Li, T., & Wang, B. (2011). The critical role of the boreal summer mean state in the development of the IOD. *Geophysical Research Letters*, *38*(2). https://doi.org/10.1029/2010GL045851

Xie, M., Wang, J.-Z., Zhang, L., & Chen, Z. (2025). Exceptional equatorial extension of extreme Indian Ocean dipole cooling: Shaping effect from strong El Niño. *Geophysical Research Letters*, *52*(2), e2024GL112464. https://doi.org/10.1029/2024GL112464

Xie, M., Wang, J.-Z., Zhang, L., Han, W., Wang, C., Fan, H., & Liu, H. (2025). Pattern asymmetry in extreme Indian Ocean dipoles shapes marine heat-height compound extremes around coastal Indonesia. *Communications Earth and Environment*, *6*(1), 229. https://doi.org/10.1038/s43247-025-02184-6

Xie, P., & Arkin, P. A. (1997). Global precipitation: A 17-year monthly analysis based on gauge observations, satellite estimates, and numerical model outputs [Dataset]. *Bulletin of the American Meteorological Society*, *78*(11), 2539–2558. https://doi.org/10.1175/1520-0477(1997)078<2539:GPAYMA>2.0.CO;2

Xu, Y., Yang, K., Sun, J., Wang, Y., He, Y.-Y., Zou, M.-J., & Jiang, Y. Z. (2023). Why was Pakistan extreme precipitation stronger in 2022 than in 2010? *Advances in Climate Change Research*, *14*(6), 913–920. https://doi.org/10.1016/j.accre.2023.11.016

References From the Supporting Information

Jin, F., & Hoskins, B. J. (1995). The direct response to tropical heating in a baroclinic atmosphere. *Journal of the Atmospheric Sciences*, *52*(3), 307–319. https://doi.org/10.1175/1520-0469(1995)052<0307:TDRTTH>2.0.CO;2

Kumar, R., Pathak, R., Sahany, S., & Mishra, S. K. (2023). Indian summer monsoon simulations in successive generations of the NCAR Community Atmosphere Model. *Theoretical and Applied Climatology*, *153*(3), 977–992. https://doi.org/10.1007/s00704-023-04514-0